crystals

MDPI

Article

Effect of High-Energy Mechanical Alloying Duration and Boron Content on the Structural and Phase Evolution of W–B Powder Mixtures

Yerkhat Dauletkhanov [1], Dias Yerbolat [1,*], Yerzhan Sapatayev [2], Leonid Izmaylov [1], Piotr Kowalewski [3], Azamat Urkunbay [1], Sardor Kambarbekov [4], Elfira Sagymbekova [1], Gulnara Yerbolatova [1,*] and Amangeldi Sagidugumar [1]

[1] Center of Excellence "VERITAS", D. Serikbayev East Kazakhstan Technical University, Ust-Kamenogorsk 070004, Kazakhstan; edauletkhanov@edu.ektu.kz (Y.D.); leonplay200415@gmail.com (L.I.); aurkunbay@edu.ektu.kz (A.U.); esagymbekova@edu.ektu.kz (E.S.); asagidugumar@ektu.kz (A.S.)
[2] Institute of Atomic Energy Branch, National Nuclear Center of the Republic of Kazakhstan, Kurchatov 180010, Kazakhstan; sapatayev@nnc.kz
[3] Faculty of Mechanical Engineering, Department of Fundamentals of Machine Design and Mechatronic Systems, Wroclaw University of Science and Technology, 50-370 Wroclaw, Poland; piotr.kowalewski@pwr.edu.pl
[4] The Research Institute "Natural Sciences, Nanotechnology and New Materials", Khoja Akhmet Yassawi International Kazakh-Turkish University, Turkestan 161200, Kazakhstan; sardor.kambarbekov@ayu.edu.kz
* Correspondence: dyerbolat@edu.ektu.kz (D.Y.); e.gulnara_77@mail.ru (G.Y.)

Abstract

Tungsten borides are promising superhard materials, but their mechanochemical synthesis requires prolonged processing, leaving the early and intermediate stages of mechanical alloying (MA) and the role of boron content largely unexplored. This study investigated the effect of boron content and high-energy MA duration (2–10 h) on the morphology, particle size distribution, and structural and phase evolution of W–B powder mixtures, comparing a near-stoichiometric W90B10 composition with a boron-excess W80B20 composition. Scanning electron microscopy, laser diffraction, X-ray diffraction, and TEM-EDS were used for characterization. The average particle size of W90B10 initially increased to 3.48 μm after 6 h and then decreased to 1.28 μm after 10 h, whereas W80B20 exhibited non-monotonic behavior, stabilizing at approximately 4.3 μm. With increasing MA duration, bcc-tungsten reflections broadened and weakened, indicating a highly disordered nanocrystalline state. Reflections of hexagonal WB_2 (crystallite size 12.5 nm) appeared in W90B10 after 8 h, whereas no crystalline boride phases were detected in W80B20 up to 10 h. TEM–EDS and SAED analyses revealed local compositional inhomogeneity and provided additional crystallographic support for the formation of nanocrystalline WB_2. These results show that boron content determines the kinetics of boride phase formation and the morphology evolution pathway during MA, identifying W90B10 as the more favorable composition for rapid nanocrystalline WB_2 synthesis.

Keywords: tungsten diboride; mechanical alloying; mechanochemical synthesis; powder morphology; phase evolution; X-ray diffraction; nanocrystalline materials; boron content

Check for updates

Academic Editor: Huan Liu

Received: 1 September 2026
Revised: 2 October 2026
Accepted: 9 October 2026
Published: 15 October 2026

Copyright: © 2026 by the authors. Licensee MDPI, Basel, Switzerland. This article is an open access article distributed under the terms and conditions of the Creative Commons Attribution (CC BY) license.

1. Introduction

Tungsten borides attract considerable attention as promising superhard materials that combine high hardness, refractoriness, and chemical stability, making them an alternative

to diamond and cubic boron nitride [1–3]. Several phases are known in the W–B system (W_2B, WB, WB_2, W_2B_5, WB_4), among which the boron-rich compounds WB_2–WB_4 are of greatest interest owing to their high hardness and thermal stability [1,2,4]. However, their practical application is limited by the difficulty of obtaining bulk forms while retaining high mechanical properties [5,6], which requires the development of effective methods for preparing highly reactive powder mixtures.

Among the methods used to produce tungsten borides, high-energy mechanical alloying (MA) is one of the most effective approaches for forming powder mixtures with high reactivity [7–9]. The rotational speed of the milling media is a key parameter governing MA efficiency: high-speed regimes provide more intensive comminution, an increased interfacial contact area, and the accumulation of structural defects that accelerate solid-state reactions [10–12]. These changes occurring during MA determine the reactivity of the powder mixture and the subsequent phase formation [13–15].

Studies of MA in the W–B system have followed two main directions. The first is concerned with the mechanochemical synthesis of tungsten boride phases. Stubičar et al. [12] investigated elemental W–B mixtures with different W:B ratios using a ball-to-powder ratio of approximately 20:1 and milling durations of up to 17 h, obtaining different tungsten boride phases depending on the initial composition. Long et al. [4] mechanically processed elemental mixtures with W:B ratios ranging from 1:4 to 1:12 for up to 40 h and detected WB_2 after milling of the W:B = 1:4 and 1:5 compositions. Huang et al. [10] showed that increasing the MA time to 20 h promoted the formation of W_2B during subsequent reactive sintering. Neov et al. [16] investigated structural changes in W_2B obtained by mechanical alloying, while Che et al. [13] obtained nanocrystalline WB_2 powders with a crystallite size of 5–10 nm after 50 h of processing. Mechanochemical routes based on WO_3–B_2O_3–Mg or $WO_{2.72}$–B_2O_3–Mg mixtures have also been employed to produce W_2B- and W_2B_5-containing powders [15,17]. However, these routes involve additional reaction products and purification procedures and therefore differ from the direct mechanical alloying of elemental W and B. Overall, previous studies employed substantially different compositions, milling equipment, ball-to-powder ratios, and processing durations, while the early-stage structural and morphological evolution of elemental W–B mixtures with different boron contents remains less systematically investigated. The second direction considers MA as a preparatory stage prior to consolidation, focusing on densification, phase formation, and the properties of the sintered materials [18–21]. In these studies, changes in the powder mixture during MA are analyzed only to the extent necessary for interpreting the consolidation results and are not regarded as an independent, controllable stage [22].

At the same time, MA is accompanied by a set of interrelated processes: plastic deformation, cold welding, agglomerate fracture, defect accumulation, crystallite size reduction, and diffraction peak broadening [11]. According to Suryanarayana [11], the balance between these processes determines the morphological evolution. Bahrami-Karkevandi et al. [23] investigated mechanochemical effects in the WO_3–B_2O_3–Mg system and showed a dependence of boride nanocomposite stability on processing duration. Nasiri-Tabrizi et al. [24] studied the effect of excess B_2O_3: WB forms at 30–50 wt.%, while WB and W_2B_5 form at 150 wt.%. However, most of these studies are limited to a processing range of 20–50 h and analyze only the initial or final state; the early and intermediate stages of MA, at which the morphology, particle size distribution, defect structure, and initial signs of boride phase formation develop, remain considerably less understood.

Of particular interest is the effect of boron content on the structural and phase evolution of W–B powder mixtures. The W90B10 composition is close to the stoichiometric composition of WB_2, which contains approximately 10.52 wt.% B, whereas W80B20 is

characterized by a substantial boron excess relative to the tungsten diboride stoichiometry. These compositions were deliberately selected as two contrasting systems: W90B10 represents a near-stoichiometric composition for WB_2 formation, whereas W80B20 represents a system with a pronounced boron excess. Their comparison under identical milling conditions allows the influence of excess boron on morphological and phase evolution to be clearly evaluated. Variation in the content of brittle boron can substantially affect the balance between agglomeration, cold welding, and particle fracture, as well as the W–B interfacial contact area and the kinetics of mechanochemical interaction. However, the effect of increased boron content on the morphological and phase evolution of the W–B system at the early stages of high-energy MA remains insufficiently understood. Reducing the duration of mechanical alloying through the use of a higher-energy regime, while retaining the nanocrystalline state of the forming boride phase, represents a relevant practical task. Understanding these processes is necessary for the informed selection of powder mixture composition and pre-activation duration prior to subsequent consolidation.

The aim of this study is to establish the regularities governing the evolution of morphology, particle size distribution, phase composition, and microstructural parameters of W–B powder mixtures during high-energy MA as a function of boron content and processing duration. In contrast to previous studies focused mainly on the final products obtained after prolonged milling or subsequent consolidation, the present work provides a time-resolved comparison of near-stoichiometric and boron-excess W–B mixtures during the early and intermediate stages of MA under identical processing conditions. The specific advance of this study lies in the combined analysis of particle morphology, particle size distribution, structural disorder, and the onset of boride-phase formation, as well as in evaluating the possibility of reducing the MA duration while retaining the nanocrystalline state of the forming boride phase. The obtained results provide a basis for the informed selection of powder composition and pre-activation duration prior to subsequent consolidation.

2. Materials and Methods

As the initial materials, elemental powders of W (purity > 99.9%, particle size < 50 μm) and B (purity > 99.9%, particle size < 50 μm) were used. The powders were supplied by Hebei Suoyi New Material Technology Co., Ltd. (Handan, China).

The initial powder mixtures with nominal compositions W90B10 and W80B20 (wt.%) were subjected to high-energy milling in a planetary ball mill (Fritsch Pulverisette 7 premium line, Fritsch GmbH, Idar-Oberstein, Germany). The ball-to-powder weight ratio was 10:1. Stainless-steel balls with a diameter of 5 mm were used as the milling media, and a stainless-steel vial with a volume of 45 mL was employed. The milling duration was set to 2, 4, 6, 8, and 10 h at a rotational speed of 1000 rpm, with 5-min pauses after every 10 min of milling to prevent local overheating inside the vials. To reduce agglomeration during milling, a small amount of stearic acid (2 wt.% of the powder mass) was added. The choice of stearic acid was based on the report of Shi et al. [25], who noted that its addition reduces diffusion and prevents cold welding of particles by forming a thin isolating film on their surface. The stearic acid was not removed after milling. As a process-control agent, it limited excessive cold welding and therefore influenced the balance between agglomeration and fracture during MA [25]. Because the same amount of stearic acid was used for both compositions, the differences observed between W90B10 and W80B20 reflect the effect of boron content under identical process-control-agent conditions. The process was carried out under an inert argon atmosphere. Loading and unloading of the powder mixtures were performed in an argon-filled glovebox to minimize oxidation. Additionally, preliminary powder mixing was conducted for 10 min at 200 rpm without the addition of stearic acid.

The crystalline structure of the milled powders was examined using an X'Pert PRO X-ray diffractometer (Malvern Panalytical, Almelo, The Netherlands) with copper anode radiation (CuKα_1, λ = 1.5406 Å). The measurement range was 20–90° 2θ, the X-ray tube voltage was 40 kV, and the current was 30 mA. The step size was 0.02°, and the counting time was 1 s per step. A fixed divergence slit of 1/2°, a divergence-slit-to-tube-focus distance of 91 mm, a fixed incident mask of 15 mm, and an antiscattering slit of 2° were used. All measurements were carried out at 25 °C. Crystal structure data for all identified phases were taken from the PDF-5+ 2026 database (International Centre for Diffraction Data, ICDD) using HighScore Plus software (version 4.9a). The average crystallite size and microstrain were determined by the isotropic Williamson–Hall (W-H) method with instrumental broadening correction. The instrumental profile function was established using a LaB_6 reference standard [26] measured under identical conditions. The physical broadening β of each reflection was extracted as:

$$\beta = \sqrt{\beta_{exp}^2 - \beta_{inst}^2} \quad (1)$$

where β_{exp} is the experimentally measured peak width, β_{inst} is the instrumental broadening determined using a reference standard, and β is the corrected physical broadening of the investigated sample. All peak-width values were converted to radians. The crystallite size and microstrain were subsequently evaluated using the classical Williamson–Hall equation:

$$\beta cos\theta = \frac{K\lambda}{D} + 4\varepsilon sin\theta \quad (2)$$

where θ is the Bragg angle, K is the shape factor (K = 0.9), λ is the Cu Kα wavelength, D is the average crystallite size, and ε is the microstrain. The values of D and ε were determined from the y-intercept and slope, respectively, of the linear dependence of $\beta\ cos\theta$ on 4 $sin\theta$.

The lattice parameter a of the bcc-W phase was calculated from the interplanar spacings d_{hkl} obtained from the fitted peak positions of the (110), (200), (211), and (220) reflections, using the relationship for a cubic crystal system:

$$a = d \cdot \sqrt{h^2 + k^2 + l^2} \quad (3)$$

where h, k, and l are the Miller indices of the corresponding reflection and d is the interplanar spacing. The lattice parameter for each sample was calculated as the arithmetic mean of the values obtained from all resolved reflections, with the standard deviation reported as the associated uncertainty.

The morphology of the initial and mechanically alloyed powder mixtures was examined by scanning electron microscopy (SEM) using a TESCAN MIRA LMS microscope (TESCAN ORSAY HOLDING, Brno, Czech Republic). Images of the powder particle surfaces were acquired in secondary electron (SE) mode. Elemental mapping of the as-mixed powders and the W90B10 powder after 8 h of MA was performed by energy-dispersive X-ray spectroscopy (EDS) coupled with SEM.

The particle size distribution of the powders was determined by laser diffraction using an Analysette 22 NeXT Nano analyzer (Fritsch GmbH, Idar-Oberstein, Germany) within a particle size range of 0.01–3800 μm. The particle-size distributions were calculated on a volume-weighted basis. To minimize powder agglomeration, the samples were dispersed in isopropyl alcohol and ultrasonically treated for 3 min prior to measurement. Each sample was measured three times, and the results are reported as the mean ± standard deviation.

The microstructure and local chemical composition of the milled powders were examined by transmission electron microscopy (TEM) using a JEM-2100 microscope (JEOL Ltd., Tokyo, Japan) equipped with a scanning transmission electron microscopy (STEM) system

and an energy-dispersive X-ray spectroscopy (EDS) system, INCA Energy TEM 350, with an X-Max 80 detector (Oxford Instruments Analytical Ltd., Abingdon, UK). Selected-area electron diffraction (SAED) patterns were acquired at an accelerating voltage of 200 kV and a nominal camera length of 100 mm, with a reciprocal-space scale bar of 0.5 nm^{-1}.

3. Results and Discussion

Analysis of the SEM images (Figures 1 and 2), particle size distribution curves (Figures 3 and 4), and the data in Table 1 show that the evolution of morphology and dispersity of the W90B10 and W80B20 powder mixtures during mechanical alloying is governed by competition between cold welding and fracture [9], with boron content acting as the key factor modulating the kinetics of these processes.

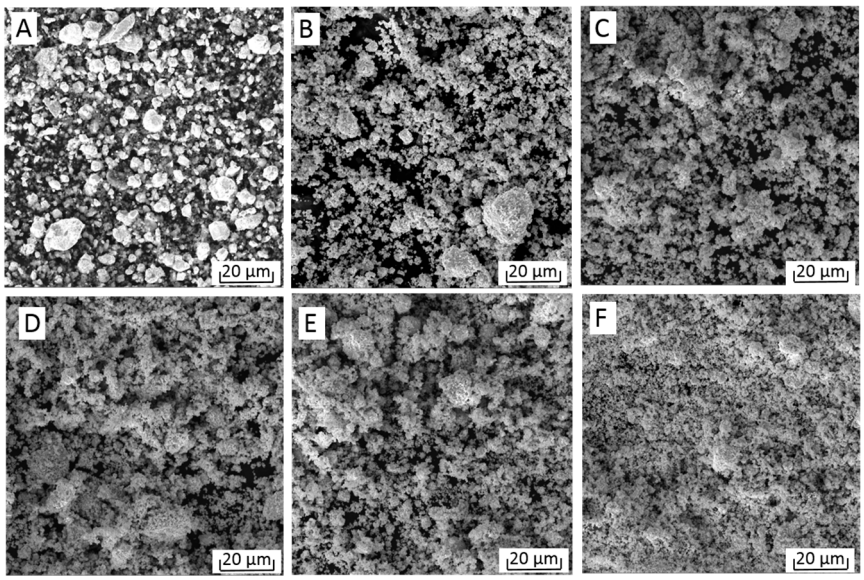


Figure 1. Morphology of the W90B10 powder mixture after different MA durations: (**A**) as-mixed; (**B**) 2 h; (**C**) 4 h; (**D**) 6 h; (**E**) 8 h; (**F**) 10 h.

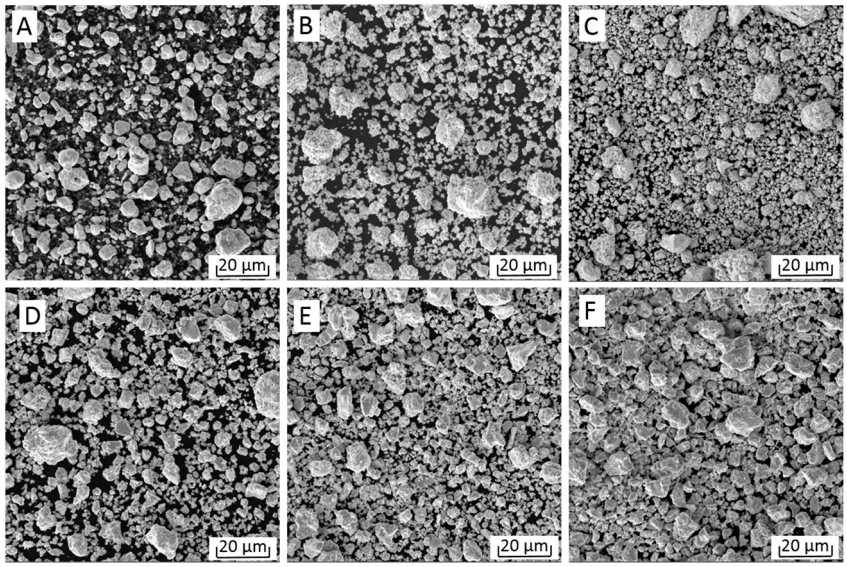


Figure 2. Morphology of the W80B20 powder mixture after different MA durations: (**A**) as-mixed; (**B**) 2 h; (**C**) 4 h; (**D**) 6 h; (**E**) 8 h; (**F**) 10 h.

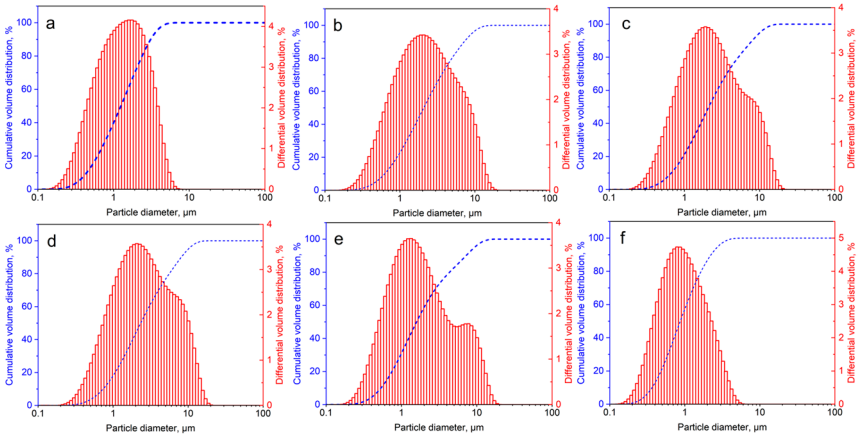


Figure 3. Particle size distribution of the W90B10 powder mixture after different MA durations: (**a**) as-mixed; (**b**) 2 h; (**c**) 4 h; (**d**) 6 h; (**e**) 8 h; (**f**) 10 h.

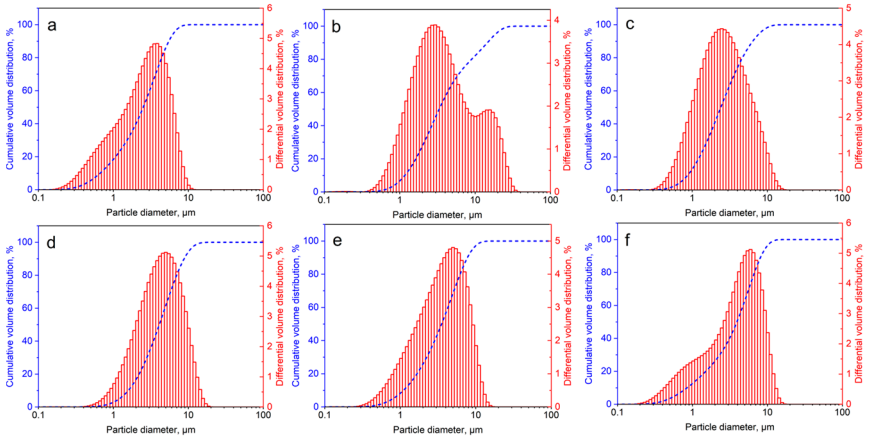


Figure 4. Particle size distribution of the W80B20 powder mixture after different MA durations: (**a**) as-mixed; (**b**) 2 h; (**c**) 4 h; (**d**) 6 h; (**e**) 8 h; (**f**) 10 h.

Table 1. Volume-weighted mean particle size of the W90B10 and W80B20 powder mixtures after different MA durations. Values are presented as the mean ± standard deviation.

Powder Mixture	As-Mixed	2 h	4 h	6 h	8 h	10 h
W90B10	1.537 ± 0.0759 μm	3.181 ± 0.0966 μm	3.457 ± 0.0462 μm	3.481 ± 0.1015 μm	2.905 ± 0.0574 μm	1.278 ± 0.1558 μm
W80B20	2.948 ± 0.0961 μm	5.917 ± 0.1517 μm	3.255 ± 0.0618 μm	4.821 ± 0.0659 μm	4.238 ± 0.1599 μm	4.278 ± 0.1614 μm

The initial mixtures exhibit a heterogeneous morphology, with coarse angular tungsten particles (10–50 μm) and submicron boron (0.5–2 μm) forming a bimodal distribution (Table 1). After 2 h of milling, cold welding dominates in both compositions, but the extent of agglomeration differs substantially: for W90B10, the average size increases to 3.18 μm, with the formation of isometric agglomerates 5–20 μm in size, whereas W80B20 forms loose conglomerates up to 50 μm with an average size of 5.92 μm. This indicates that excess boron intensifies the initial welding stage by increasing the interfacial contact area [23].

For W90B10, densification and agglomerate growth are observed within the 4–6 h interval, reaching a maximum of 3.48 μm at 6 h, after which a qualitative transition occurs: brittle fracture begins to dominate at 8 h, decreasing the average size to 2.91 μm, and by 10 h a highly dispersed system with particles of 0.5–3 μm and an average size of 1.28 μm is formed (Table 1). This two-stage evolution is consistent with the literature data [4,10], where longer mechanical alloying times lead to effective size reduction and increased powder reactivity.

In contrast to the near-stoichiometric W90B10, the W80B20 mixture exhibits a non-monotonic change in average particle size: an increase to 5.92 μm at 2 h is followed by a decrease to 3.26 μm at 4 h, a subsequent increase to 4.82 μm at 6 h, and stabilization at approximately 4.3 μm after 8–10 h of processing. The final average particle size of W80B20 after 10 h exceeds the corresponding value for W90B10 by more than a factor of three. This behavior indicates that increasing the boron content changes the balance between cold welding and fracture, resulting in the retention of comparatively larger agglomerates.

All morphological transitions correlate closely with changes in the particle size distribution curves: the appearance of fragmented shapes at 8 h in W90B10 coincides with the disappearance of the tail above 10 μm (Figures 1E and 3e), while the renewed agglomerate growth at 6 h in W80B20 is reflected in a broadening of the distribution toward coarser fractions (Figures 2D and 4d). The fine-grained state of W90B10 after 10 h, with a highly developed interfacial surface, provides favorable conditions for solid-state diffusion during subsequent spark plasma sintering [3,12]. Boron content therefore determines the trajectory of structural modification of the powder mixture, which must be taken into account in the targeted design of mechanochemical synthesis processes for tungsten borides.

The diffraction patterns of the initial W90B10 and W80B20 powder mixtures (Figure 5, as-mixed curves) contain reflections at $2\theta \approx 40.3°$, 58.3°, 73.2°, and 87.1°, corresponding to the (110), (200), (211), and (220) crystallographic planes of body-centered cubic (bcc) tungsten with the Im-3m space group, according to ICDD PDF card 04-003-6204. No reflections of crystalline boride phases were detected in the initial mixtures, indicating the absence of interaction between the components at the mixing stage and the preservation of the initial crystalline structure of W regardless of boron content. At the same time, the absence of boron and boride reflections does not exclude the presence of amorphous boron and possible X-ray-amorphous products, whose content lies below the detection limit of the XRD method.

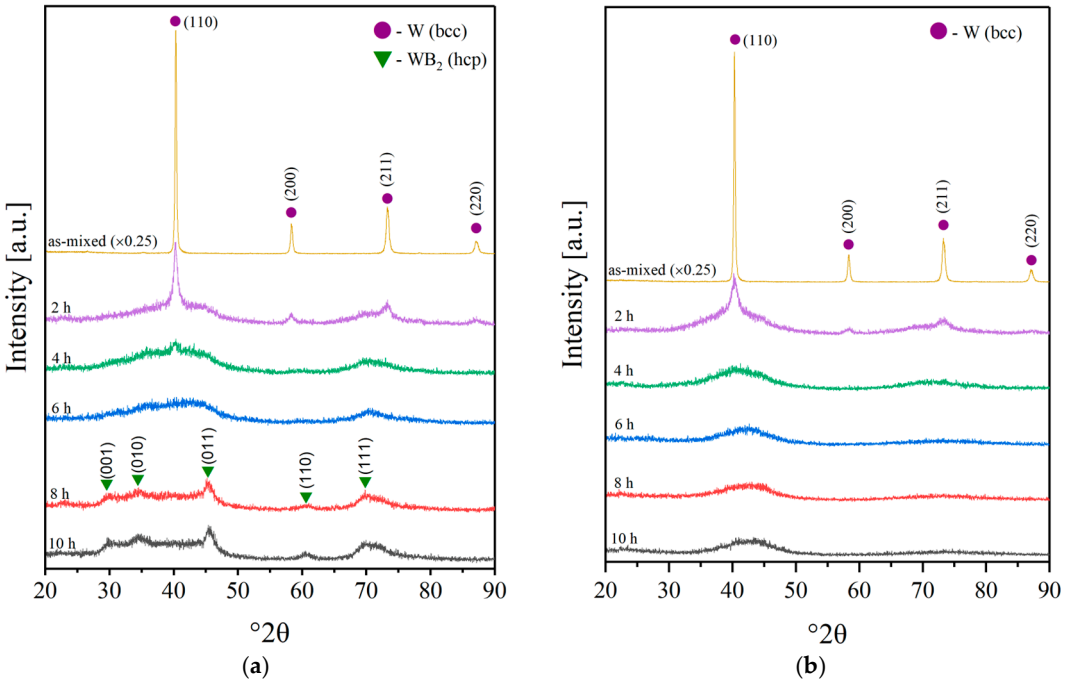


Figure 5. X-ray diffraction patterns of the W90B10 and W80B20 powder mixtures after different MA durations: (**a**) W90B10; (**b**) W80B20.

After 2 h of MA, both compositions show a systematic broadening and decrease in intensity of the tungsten reflections, typical of the early stage of mechanical alloying and

attributed to crystallite refinement and the accumulation of microstrain and lattice defects resulting from intensive plastic deformation [11].

With increasing processing time up to 4–6 h, the diffraction patterns of both compositions transform into a broad diffuse halo in the region of the (110) reflection, while the narrow (200), (211), and (220) reflections practically disappear, indicating a transition to a highly disordered state with loss of long-range crystalline order due to critical defect accumulation and a reduction in bcc-W crystallite size below the coherent scattering threshold [11]. This evolution is typical of high-energy MA of refractory metals and reflects a transition from a crystalline to a highly disordered state.

Further increases in MA duration reveal differences in the phase evolution of the compositions studied. For the W90B10 powder mixture, weak features appear after 8 h of processing at $2\theta \approx 29.3^\circ$, 34.3°, 45.7°, 61.3°, and 69.4°, superimposed on the broad diffraction maxima. The positions of these maxima correspond to the (001), (100), (101), (110), and (111) reflections of the hexagonal WB_2 phase with the P6/mmm space group, according to ICDD PDF card 04-003-6624. In the region of $2\theta \approx 61^\circ$, overlapping of the closely spaced (002) and (110) reflections, located at 60.678° and 61.345°, respectively, is possible. The considerable broadening of the identified maxima indicates a nanocrystalline and highly defective state of the forming boride phase. The corresponding diffraction features persist after 10 h of processing, indicating the continued presence of WB_2 in the mechanically alloyed mixture. The formation of WB_2 at this stage is consistent with the results of Long et al. [4], who demonstrated the feasibility of mechanochemical synthesis of tungsten borides upon prolonged processing of W–B mixtures.

In contrast to W90B10, no crystalline boride reflections were detected in the W80B20 mixture even after 8 and 10 h of MA (Figure 5b)—the diffraction patterns retain the appearance of a broad amorphous halo, with no evidence of WB_2 or other crystalline compound formation. This difference indicates that the higher boron content modifies the phase-evolution pathway of the W–B mixture under the investigated milling conditions. In addition, excess boron on the surface of the tungsten particles may hinder the ordering of the boride crystal structure, stabilizing a highly disordered state of the mixture with suppressed long-range crystalline order up to 10 h of processing [23].

The XRD data (Figure 5) show that, regardless of composition, mechanical alloying leads to a consistent transformation of the W–B powder mixtures from a crystalline to a highly disordered state with loss of long-range crystalline order; however, the kinetics and completeness of the subsequent mechanochemical crystallization of the WB_2 phase depend substantially on boron content: in the composition with lower boron content (W90B10), the crystalline WB_2 phase forms already during MA, whereas the boron excess in W80B20 stabilizes the amorphous state up to 10 h of processing—a factor that must be taken into account when selecting the optimal composition for subsequent spark plasma sintering.

To quantitatively describe the evolution of the defect structure and refine the crystal lattice parameters at the identified stages, the Williamson–Hall method was applied, and the results are presented in Figures 6 and 7 and Table 2. It should be noted that the crystallite sizes and microstrains of the W90B10 and W80B20 samples after 4 and 6 h of mechanical alloying were not quantitatively evaluated using the Williamson–Hall method. This is because the diffraction patterns at these stages transform into a broad diffuse halo, while the narrow reflections of bcc-W almost completely disappear (Figure 5), indicating a transition to a highly disordered state with the loss of long-range crystalline order and making the correct application of the W–H method impossible [9].

Following 2 h of MA, both compositions exhibit a systematic decrease in the average crystallite size of W and an increase in microstrain. In W80B20, the average crystallite size (D) decreases from 107.4 to 29.1 nm, while the microstrain (ε) increases from 0.0021

to 0.0111. In W90B10, D decreases from 81.6 to 34.4 nm, while ε increases from 0.0017 to 0.0101. Such intensive refinement and defect accumulation at the initial stage of MA are attributed to the repeated plastic deformation of particles during collisions with the milling media, leading to the generation and multiplication of dislocations, their rearrangement into subgrain boundary walls, and, consequently, the fragmentation of the initially large W crystallites into smaller coherent scattering domains.

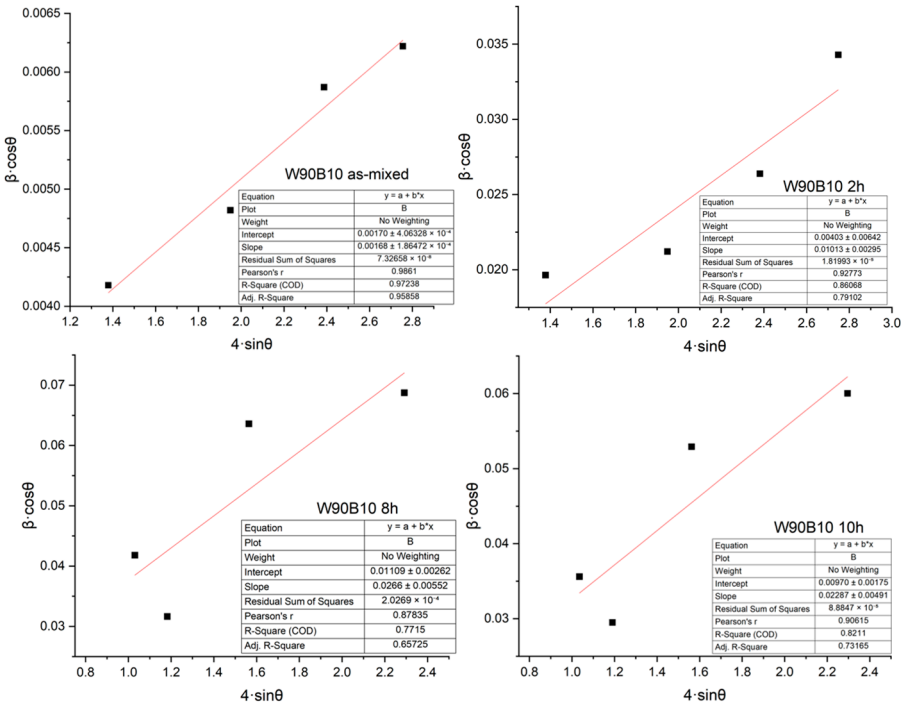


Figure 6. Williamson–Hall plots for W90B10 powder mixture at different MA durations.

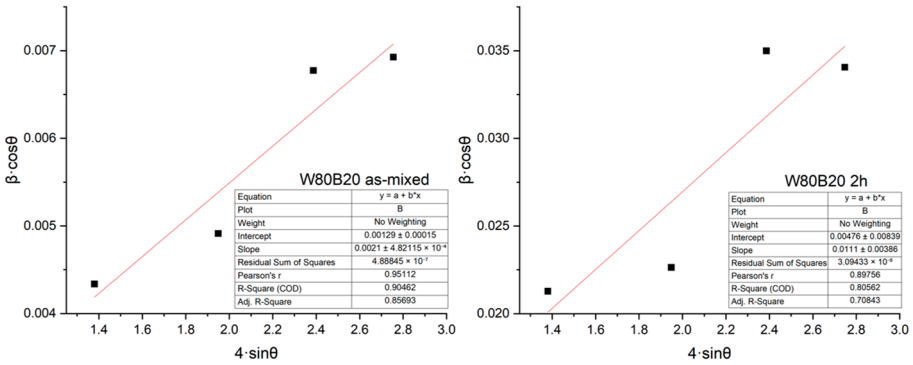


Figure 7. Williamson-Hall plots for W80B20 powder mixture at different MA durations.

Table 2. Average crystallite size (D) and microstrain (ε) of the W and WB_2 phases and lattice parameter (a) of the W phase as a function of powder composition and MA duration, calculated using Equations (1)–(3).

Powder Mixture	MA Time (h)	Phase	D (nm)	ε	a (Å)
W80B20	as-mixed	W	107.4 ± 12.5	0.0021 ± 0.0005	3.1622 ± 0.0007
	2	W	29.1 ± 5.1	0.0111 ± 0.0039	3.1714 ± 0.0222
W90B10	as-mixed	W	81.6 ± 2.0	0.0017 ± 0.0002	3.1614 ± 0.0007
	2	W	34.4 ± 5.5	0.0101 ± 0.0030	3.1648 ± 0.0023
	8	WB_2	12.5 ± 2.9	0.0266 ± 0.0055	–
	10	WB_2	14.3 ± 2.6	0.0229 ± 0.0049	–

A comparison of the compositions after 2 h shows that the W crystallites in W80B20 undergo slightly more intensive refinement than those in W90B10, with a comparable but slightly higher level of accumulated microstrain. This trend indicates that particle-size evolution and crystallite refinement occur at different structural scales and do not necessarily follow the same pattern. After 2 h of MA, W80B20 exhibits a smaller W crystallite size and a slightly higher microstrain than W90B10, despite its larger average particle size. Thus, the increased boron content is associated with more pronounced early-stage crystallite refinement without a corresponding reduction in the size of the powder agglomerates.

The calculated lattice parameter of W showed that, in the initial mixtures, a was nearly identical to the reference value of 3.1652 Å (ICDD 04-003-6204), amounting to 3.1622 ± 0.0007 Å for W80B20 and 3.1614 ± 0.0007 Å for W90B10. The small differences between the experimental and reference values are within the order of the experimental error and do not indicate significant distortion of the initial tungsten lattice. After 2 h of mechanical alloying, the calculated lattice parameter was 3.1714 ± 0.0222 Å for W80B20 and 3.1648 ± 0.0023 Å for W90B10. Only a slight change relative to the reference value was observed for W90B10. For W80B20, the mean value was somewhat higher; however, the considerable standard deviation does not allow this difference to be unambiguously interpreted as a statistically significant expansion of the crystal lattice. Therefore, the broadening of the diffraction reflections, reduction in the size of the coherent scattering domains, and increase in the calculated microstrain should be regarded as the primary evidence of defect accumulation after 2 h of treatment.

The WB_2 phase formed in W90B10 after 8 h of MA exhibited the smallest crystallite size recorded for this phase, 12.5 nm, and the highest microstrain level, 0.0266. This is characteristic of a highly nonequilibrium nanocrystalline structure newly formed through the mechanochemical reaction $W + 2B \rightarrow WB_2$. The exothermic solid-state reaction initiated by local impact heating simultaneously generates numerous nuclei of the new phase, thereby determining their initially small size and high defect density. With further treatment for up to 10 h, the opposite trend was observed: the crystallite size of WB_2 increased to 14.3 nm, while the microstrain decreased to 0.0229. This change is consistent with partial relaxation of the defect structure and modest crystallite growth of the already formed WB_2 phase during continued milling. Such evolution may result from a dynamic balance between defect accumulation and structural recovery, potentially assisted by transient local temperature increases at the collision sites. Continued mechanical treatment may also promote the rearrangement and coalescence of adjacent coherent domains, resulting in a lower microstrain and a slightly larger average crystallite size. The detection of WB_2-related reflections after 8 h of mechanical alloying indicates comparatively rapid boride formation under the present high-energy milling conditions. In comparison, Che et al. [13] reported the formation of nanocrystalline WB_2 after 50 h of mechanical alloying, with a crystallite size of 5–10 nm, whereas Long et al. [4] employed milling durations of up to 40 h for elemental W–B mixtures. Although the reported studies differ in composition, milling equipment, ball-to-powder ratio, and process-control conditions, the present results demonstrate that the applied milling regime enables detectable nanocrystalline WB_2 formation within a substantially shorter processing time.

The quantitative data presented in Table 2 confirm and further detail the qualitative interpretation derived from the analysis of Figure 5. In both compositions, MA is accompanied by progressive refinement of the W crystallites and accumulation of microstrain up to the loss of long-range crystalline order, with the kinetics of this process being slightly more pronounced in W80B20. The subsequent mechanochemical crystallization of the WB_2 phase in W90B10 proceeds through a stage of maximum structural nonequilibrium after 8 h, followed by partial relaxation after 10 h.

To confirm the presence of boron in the initial mixtures, SEM-EDS elemental mapping was performed for the as-mixed W90B10 and W80B20 powders (Figure 8). The maps show a broadly distributed boron signal throughout the analyzed areas of both compositions, with no pronounced boron-rich agglomerates at the micrometer scale. This indicates that preliminary mixing provides extensive contact between the W and B components at the micrometer scale, despite the absence of detectable crystalline boron reflections in the XRD patterns of the as-mixed powders.

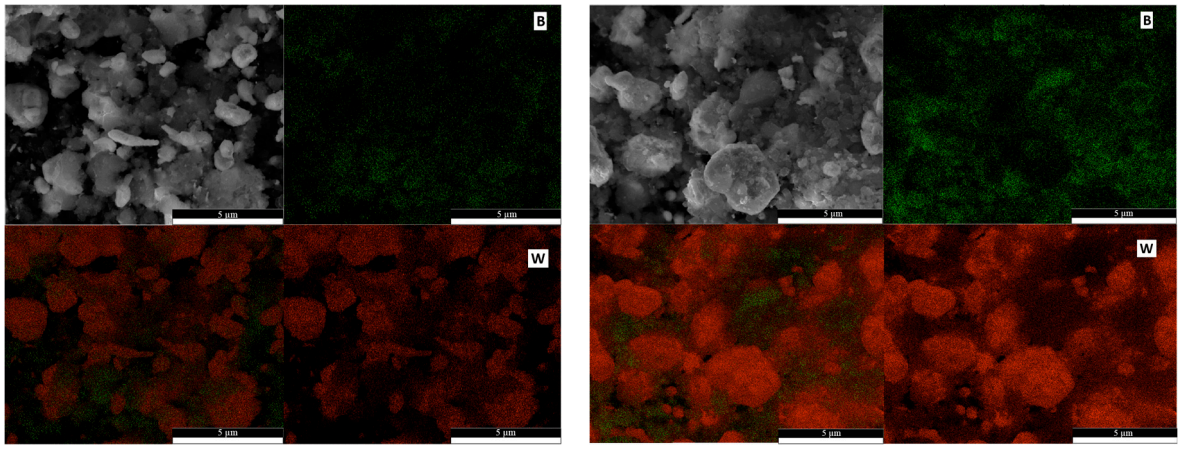


Figure 8. SEM-EDS elemental mapping of the as-mixed powders: (**a**) W90B10; (**b**) W80B20.

To examine the elemental distribution at different scales, SEM-EDS and TEM-EDS analyses were performed for the W90B10 powder after 8 h of MA, i.e., at the MA duration at which WB_2 reflections first appear in the XRD patterns (Figure 5). SEM–EDS mapping (Figure 9) shows a broadly distributed W and B signal over the analyzed particle surfaces, with no pronounced boron-rich agglomerates at the micrometer scale. The oxygen signal remains weak and homogeneous, indicating only minor surface oxidation, consistent with the inert atmosphere used during milling and handling. These results indicate that, at the micrometer scale, MA provides a well-developed W–B interfacial contact area favorable for mechanochemical interaction.

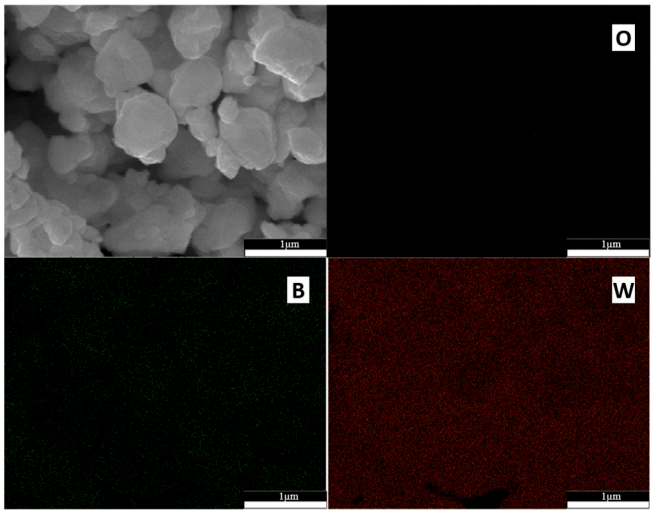


Figure 9. SEM–EDS elemental mapping of the W90B10 powder mixture after 8 h of MA.

It should be noted, however, that the apparently uniform distribution of boron in the SEM-EDS maps reflects the micrometer-scale spatial resolution of the method, which

averages the signal over regions containing both W and B particles. To overcome these limitations and obtain local information on the nanoscale distribution of boron, TEM-EDS was employed, enabling local compositional analysis of individual powder regions at the nanoscale (Figure 10 and Table 3). The original high-resolution version of Figure 10 is provided as Figure S1 in the Supplementary Materials. The TEM-EDS results reveal an inhomogeneous elemental distribution. The boron content ranges from below the detection limit in Spectrum 2 to 25.83 wt.% in Spectrum 5, the oxygen content ranges from 1.28 to 3.59 wt.%, and the tungsten content ranges from 71.14 to 96.41 wt.%. Spectra 1 and 4 contain 11.00 and 9.01 wt.% B, respectively; these values are close to the calculated boron content in stoichiometric WB_2 (approximately 10.52 wt.%) and may therefore correspond to regions with compositions close to that of tungsten diboride. The increased boron contents in Spectra 3 and 5 (21.78 and 25.83 wt.%, respectively) indicate B-enriched regions that may contain unreacted boron together with W–B-containing regions. Spectrum 2, containing 96.41 wt.% W with no reliably detectable boron signal, corresponds predominantly to a tungsten-rich region, confirming that the boride-forming reaction remains incomplete and proceeds inhomogeneously after 8 h.

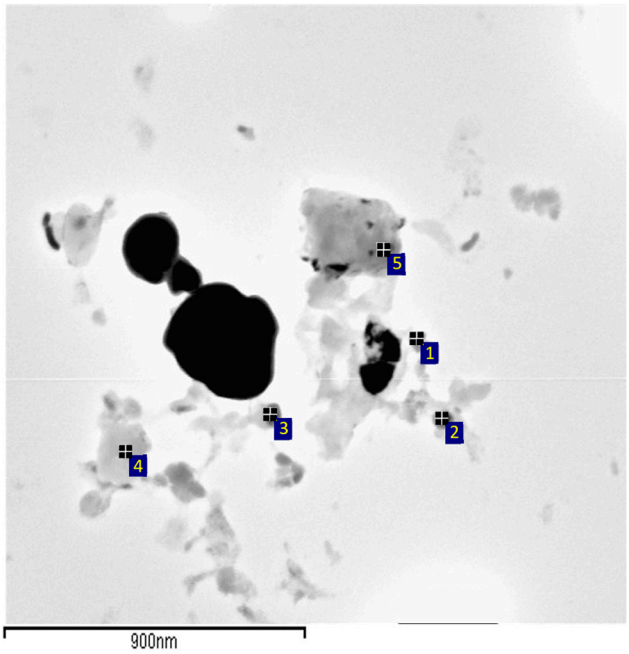


Figure 10. TEM image of the W90B10 powder mixture after 8 h of mechanical alloying indicating the regions selected for local EDS analysis. Magnification: 60,000×.

Table 3. Local elemental composition of the W90B10 powder mixture after 8 h of mechanical alloying according to TEM-EDS analysis, wt.%.

Spectrum	B	O	W	Total
Spectrum 1	11.00	1.28	87.72	100.00
Spectrum 2	not detected	3.59	96.41	100.00
Spectrum 3	21.78	2.36	75.86	100.00
Spectrum 4	9.01	3.18	87.81	100.00
Spectrum 5	25.83	3.03	71.14	100.00

Thus, the SEM-EDS and TEM-EDS results are not contradictory but reflect different levels of spatial averaging: a relatively homogeneous W–B distribution at the micrometer scale, and an incomplete, locally inhomogeneous boride formation at the nanometer scale. The low oxygen content of 1.28–3.59 wt.% in all spectra indicates minimal oxidation of

the particle surfaces, achieved by loading and unloading the powders under an argon atmosphere. Although stainless-steel milling media may introduce Fe- or Cr-containing impurities through wear, no Fe- or Cr-containing crystalline phases were identified by XRD, and no Fe or Cr signals were detected in the analyzed TEM-EDS regions. In addition, no carbon signal attributable to stearic acid was detected by TEM-EDS, and no crystalline carbon-containing phases were identified by XRD. The TEM-EDS data reveal local regions with boron contents close to the stoichiometric composition of WB_2 and are consistent with the assignment of the weak diffraction maxima in Figure 5 to the hexagonal WB_2 phase.

To obtain crystallographic evidence for the formation of the WB_2 phase, SAED was performed on the W90B10 powder after 8 h of MA (Figure 11), and the measured interplanar spacings were compared with the reference data for hexagonal WB_2 and bcc-W (Table 4). The reflections P3 and P4 with d = 1.3532 Å match the (111) reflection of WB_2, while P8 and P9 with d = 1.2018 Å correspond to the (201) reflection of WB_2. The reflections P1, P2a, P2b, and P5 with d = 1.5250 and 3.0500 Å correspond to the (002) and (001) reflections of WB_2, respectively. The reflections P6 and P7 with d = 1.5815 Å are assigned to the (200) reflection of residual bcc-W. These results provide additional crystallographic support for the presence of nanocrystalline WB_2 in the mechanically alloyed W90B10 powder after 8 h, in agreement with the weak and broadened WB_2 reflections detected by XRD at the same processing duration. The residual bcc-W reflections detected by SAED were not resolved in the XRD patterns because of the strong refinement and microstrain of the W crystallites, and their presence is consistent with the W-rich regions revealed by TEM-EDS after 8 h of MA.

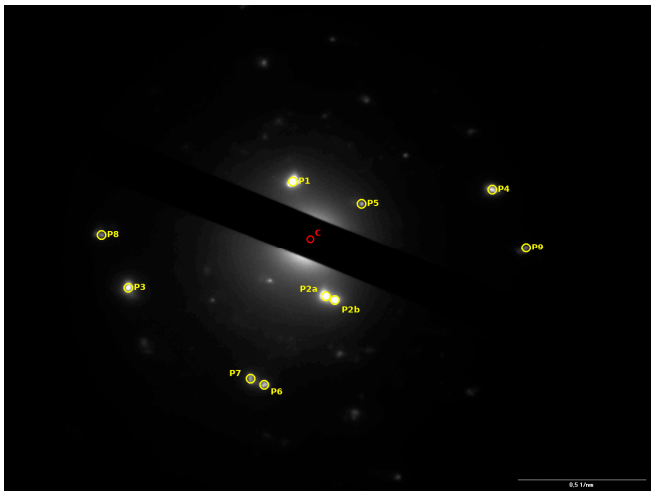


Figure 11. SAED pattern of the W90B10 powder mixture after 8 h of mechanical alloying. The reconstructed diffraction center (C) and selected reflections (P1–P9) used for phase identification are indicated.

Table 4. Quantitative parameters of selected diffraction reflections.

Spot	d (Å)	Phase	(hkl)
P1	1.5252	WB_2	(002)
P2a	1.5252	WB_2	(002)
P2b	3.0501	WB_2	(001)
P3	1.3533	WB_2	(111)
P4	1.3533	WB_2	(111)
P5	3.0501	WB_2	(001)
P6	1.5816	W	(200)
P7	1.5816	W	(200)
P8	1.2017	WB_2	(201)
P9	1.2017	WB_2	(201)

4. Conclusions

It was established that high-energy mechanical alloying induces successive morphological and structural–phase modifications in W–B powder mixtures, the nature of which strongly depends on the boron content. For the W90B10 composition, following the initial growth of agglomerates, their fragmentation becomes predominant, resulting in the formation of the most highly dispersed state after 10 h. For the W80B20 composition with a significant excess of boron, a non-monotonic variation in the average particle size and the retention of larger agglomerates were observed, indicating a different balance between agglomeration and fragmentation processes.

It was established that, with increasing mechanical alloying duration, the bcc-W reflections gradually broaden and decrease in intensity owing to a reduction in crystallite size, the accumulation of microstrain, and the formation of a highly disordered nanocrystalline state. The subsequent phase evolution of the investigated compositions was shown to differ. In the W90B10 powder mixture, reflections of the hexagonal WB_2 phase appear after 8 h, indicating the initiation of the mechanochemical interaction between W and B directly during milling. In the W80B20 composition, distinct reflections of crystalline boride phases are not detected for treatment durations of up to 10 h. SEM–EDS mapping confirmed the presence and broad distribution of boron in the initial powder mixtures, while TEM–EDS revealed local chemical inhomogeneity in the W90B10 powder after 8 h of MA, indicating that the boride-forming reaction remained incomplete. The interplanar spacings determined from the SAED pattern were consistent with the reflections of hexagonal WB_2 and residual bcc-W, providing additional crystallographic support for the XRD-based phase identification.

It was shown that the use of the high-energy regime enables the formation of the nanocrystalline WB_2 phase in the W90B10 composition to be initiated after only 8 h of mechanical alloying, thereby reducing the duration of the mechanochemical preparation of W–B powder mixtures. It was established that, within the investigated treatment interval, the W90B10 composition is more suitable for obtaining nanocrystalline tungsten diboride, whereas the significant excess of boron in W80B20 does not promote the formation of crystalline boride phases. The obtained results may be used to select the composition and preliminary mechanical alloying regime of W–B powders prior to subsequent consolidation.

Supplementary Materials: The following supporting information can be downloaded at https://www.mdpi.com/article/10.3390/cryst16100666/s1, Figure S1: Original high-resolution version of Figure 10.

Author Contributions: Conceptualization, D.Y., Y.S. and Y.D.; methodology, D.Y., Y.D. and Y.S.; software, D.Y., L.I., E.S. and Y.S.; validation, D.Y., Y.D., S.K., G.Y., A.S. and P.K.; formal analysis, D.Y., Y.S. and L.I.; investigation, D.Y., Y.D., L.I., A.U., S.K., E.S., and A.S.; resources, Y.D., A.U., A.S. and P.K.; data curation, D.Y., G.Y. and Y.S.; writing—original draft preparation, D.Y., L.I. and Y.D.; writing—review and editing, D.Y., Y.D., P.K., G.Y. and Y.S.; visualization, D.Y. and Y.S.; supervision, Y.D. and D.Y.; project administration, D.Y. and Y.D. All authors have read and agreed to the published version of the manuscript.

Funding: This research was funded by the Science Committee of the Ministry of Science and Higher Education of the Republic of Kazakhstan (Grant No. BR24992854).

Data Availability Statement: The data presented in this study are available from the corresponding author upon reasonable request.

Acknowledgments: During the preparation of this manuscript, the authors used ChatGPT (GPT-5), a generative artificial intelligence tool developed by OpenAI, for English-language editing and improvement of the clarity and readability of the text. The authors reviewed and edited the generated content and take full responsibility for the final content of the manuscript.

Conflicts of Interest: The authors declare no conflicts of interest.

References

1. Poligenko, A.V.; Ruban, E.A.; Osipov, K.M.; Shaporenkov, A.A.; Dushik, V.V. Tungsten borides: A review of phase stability, properties, synthesis, and applications. *Solids* **2026**, *7*, 15. [CrossRef]
2. Mohammadi, R.; Xie, M.; Lech, A.T.; Turner, C.L.; Kavner, A.; Tolbert, S.H.; Kaner, R.B. Toward inexpensive superhard materials: Tungsten tetraboride-based solid solutions. *Proc. Natl. Acad. Sci. USA* **2011**, *108*, 10958–10962. [CrossRef] [PubMed]
3. Bykova, E.; Ovsyannikov, S.; Bykov, M.; Yin, Y.; Fedotenko, T.; Holz, H.; Gabel, S.; Merle, B.; Chariton, S.; Prakapenka, V.B.; et al. Synthesis, crystal structure, and properties of stoichiometric hard tungsten tetraboride, WB_4. *J. Mater. Chem. A* **2022**, *10*, 16809–16818. [CrossRef]
4. Long, Y.; Zhang, F.; Lin, H.-T. Mechanochemical synthesis and annealing of tungsten di- and tetra-boride. *J. Am. Ceram. Soc.* **2020**, *103*, 1256–1265. [CrossRef]
5. Liu, Y.; Liu, X.; Lai, C.; Ma, J.; Meng, X.; Zhang, L.; Xu, G.; Lu, Y.; Li, H.; Wang, J.; et al. Boriding of tungsten by the powder-pack process: Phase formation, growth kinetics and enhanced neutron shielding. *Int. J. Refract. Met. Hard Mater.* **2023**, *110*, 106049. [CrossRef]
6. Windsor, C.G.; Astbury, J.O.; Morgan, J.G.; Wilson, C.L.; Humphry-Baker, S.A. Activation and transmutation of tungsten boride shields in a spherical tokamak. *Nucl. Fusion* **2022**, *62*, 036009. [CrossRef]
7. Fahrenholtz, W.G.; Hilmas, G.E.; Talmy, I.G.; Zaykoski, J.A. Refractory diborides of zirconium and hafnium. *J. Am. Ceram. Soc.* **2007**, *90*, 1347–1364. [CrossRef]
8. Mukhamedova, N.; Yerbolat, D.; Zakerov, S.; Dauletkhanov, Y.; Urkunbay, A.; Yerbolatova, G. Effect of Mechanical Alloying Time on the Structural and Phase State of BN–C–Ti–Al Composites as Structural Prerequisites for Hydrogen Storage. *Crystals* **2026**, *16*, 155. [CrossRef]
9. Tabiyeva, Y.; Yerbolat, D.; Zakerov, S.; Dauletkhanov, Y.; Urkunbay, A.; Sagymbekova, E.; Kantay, N. Effect of Titanium Content and Mechanical Alloying Time on the Formation of Nanocrystalline Solid Solutions in the Ni–Al–Ti System. *Crystals* **2026**, *16*, 71. [CrossRef]
10. Huang, W.; Li, J.; Liu, Y. Reactive synthesis of W_2B alloy powder based on mechanical alloying, Rare Met. *Mater. Eng.* **2025**, *54*, 1335–1343. [CrossRef]
11. Suryanarayana, C. Mechanical alloying and milling. *Prog. Mater. Sci.* **2001**, *46*, 1–184. [CrossRef]
12. Stubičar, N.; Tonejc, A.; Stubičar, M. X-ray diffraction study of W–B elemental powder mixtures after high-energy ball-milling. *Fiz. A A J. Exp. Theor. Phys.* **1995**, *4*, 65–76. Available online: https://hrcak.srce.hr/303103 (accessed on 8 October 2026).
13. Che, J.; Long, Y.; Zheng, X.; Lin, H.-T.; Plucknett, K. Mechanical alloying assisted spark plasma sintering of tungsten diboride ceramics. *Mater. Chem. Phys.* **2019**, *237*, 121848. [CrossRef]
14. Aubakirova, D.; Sagymbekova, E.; Kozhakhmetov, Y.; Dauletkhanov, Y.; Urkunbay, A.; Yerbolat, D.; Kowalewski, P.; Tabiyeva, Y. Evolution of the Structural and Phase Composition of Ni–Ti–Cu Alloy Produced via Spark Plasma Sintering After Aging. *Crystals* **2025**, *15*, 939. [CrossRef]
15. Coşkun, S.; Öveçoğlu, M.L. Room-temperature mechanochemical synthesis of W_2B_5 powders. *Metall. Mater. Trans. A* **2013**, *44*, 1805–1813. [CrossRef]
16. Neov, D.; Slavov, L.; Donkov, A.A.; Mirzayev, M.N.; Popov, E.; Demir, E.; Siemek, K.; Djourelov, N.; Turchenko, V.A.; Sharipov, Z.A.; et al. Structural study of W_2B obtained via mechanical alloying of W, B_4C, TiC and graphite before and after He ions irradiation. *Nucl. Instrum. Methods Phys. Res. B* **2020**, *479*, 45–52. [CrossRef]
17. Süzer, İ.; Akbari, A.; Kaya, F.; Mertdinç-Ülküseven, S.; Derin, B.; Öveçoğlu, M.L.; Ağaoğulları, D. Room-temperature synthesis of refractory borides: A case study on mechanochemistry and characterization of Mo-borides and W-borides. *Ceram. Int.* **2025**, *51*, 20518–20531. [CrossRef]
18. Munir, Z.A.; Anselmi-Tamburini, U.; Ohyanagi, M. The effect of electric field and pressure on the synthesis and consolidation of materials: A review of the spark plasma sintering method. *J. Mater. Sci.* **2006**, *41*, 763–777. [CrossRef]
19. Tokita, M. Development of advanced spark plasma sintering (SPS) systems and its industrial applications. In *Pulse Electric Current Synthesis and Processing of Materials*; Munir, Z.A., Anselmi-Tamburini, U., Eds.; Wiley: Hoboken, NJ, USA, 2006.
20. Khor, K.A.; Yu, L.G.; Sundararajan, G. Formation of hard tungsten boride layer by spark plasma sintering boriding. *Thin Solid Films* **2005**, *478*, 232–237. [CrossRef]
21. Lin, S.; Long, Y.; Wang, Y.; Lin, H.-T. WB_2 ceramics prepared by combination of boro/carbothermal reduction process and spark plasma sintering: Effect of C content and sintering rate. *J. Eur. Ceram. Soc.* **2024**, *44*, 7566–7571. [CrossRef]
22. Matějíček, J.; Vilémová, M.; Veverka, J.; Kubásek, J.; Lukáč, F.; Novák, P.; Preisler, D.; Stráský, J. On the structural and chemical homogeneity of spark plasma sintered tungsten. *Metals* **2019**, *9*, 879. [CrossRef]
23. Bahrami-Karkevandi, M.; Ebrahimi-Kahrizsangi, R.; Nasiri-Tabrizi, B. Formation and stability of tungsten boride nanocomposites in WO_3–B_2O_3–Mg ternary system: Mechanochemical effects. *Int. J. Refract. Met. Hard Mater.* **2014**, *46*, 117–124. [CrossRef]

24. Nasiri-Tabrizi, B.; Ebrahimi-Kahrizsangi, R.; Bahrami-Karkevandi, M. Effect of excess boron oxide on the formation of tungsten boride nanocomposites by mechanically induced self-sustaining reaction. *Ceram. Int.* **2014**, *40*, 14235–14246. [CrossRef]
25. Shi, J.; Zheng, A.; Lin, Z.; Chen, R.; Zheng, J.; Cao, Z. Effect of process control agent on alloying and mechanical behavior of L21 phase Ni–Ti–Al alloys. *Mater. Sci. Eng. A* **2018**, *740*, 130–136. [CrossRef]
26. *NIST SRM 660b*; Line Position and Line Shape Standard for Powder Diffraction (Lanthanum Hexaboride Powder). National Institute of Standards and Technology: Gaithersburg, MD, USA, 2010.

Disclaimer/Publisher's Note: The statements, opinions and data contained in all publications are solely those of the individual author(s) and contributor(s) and not of MDPI and/or the editor(s). MDPI and/or the editor(s) disclaim responsibility for any injury to people or property resulting from any ideas, methods, instructions or products referred to in the content.